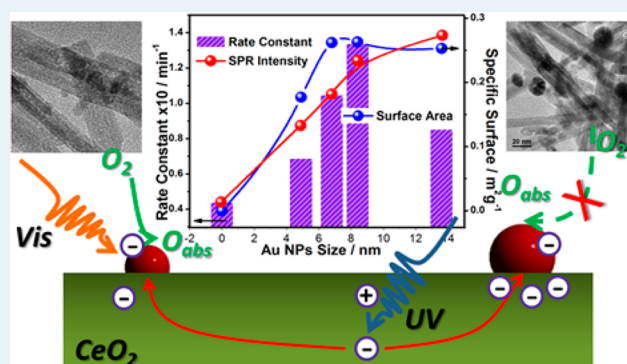


Equilibrating the Plasmonic and Catalytic Roles of Metallic Nanostructures in Photocatalytic Oxidation over Au-Modified CeO<sub>2</sub>Dong Jiang,<sup>†,‡</sup> Wenzhong Wang,<sup>\*,†</sup> Songmei Sun,<sup>†</sup> Ling Zhang,<sup>†</sup> and Yali Zheng<sup>†,‡</sup><sup>†</sup>State Key Laboratory of High Performance Ceramics and Superfine Microstructure, Shanghai Institute of Ceramics, Chinese Academy of Sciences, 1295 Dingxi Road, Shanghai 200050, People's Republic of China<sup>‡</sup>University of Chinese Academy of Sciences, Beijing 100049, People's Republic of China

## Supporting Information

**ABSTRACT:** Finite amounts of noble metals have been widely introduced as surface plasmon resonance (SPR) mediators and reductive cocatalysts for solar-driven energy conversion. At present, knowledge of the roles of metal loading is multifarious and may be one-sided in some cases. In addition, the catalytic roles which metals play in photocatalytic oxidation have been rarely discussed. It is necessary to explore the equilibrium between plasmon resonance and surface catalysis over metallic nanostructures. Herein, Au NPs with various loading amounts (0.25–1 wt %) and particle sizes (3–20 nm) were attached to CeO<sub>2</sub> by photodeposition. Aerobic oxidations of propylene under simulated sunlight and visible (>420 nm) light irradiation were selected as probe reactions. Both processes exhibited similar humplike activity dependence upon Au NP addition, with a peak at 0.67 wt % loading and a size of 8.4 nm. Modifications to the whole photocatalytic process brought by metal attachment have been integrally examined, concerning both the photoexcitation and surface catalysis steps. With an increase of Au loading, the induced SPR photoabsorption, charge separation, and resonant energy transfer were enhanced, whereas outgrown Au NPs (>10 nm) led to the saturation of exposed active sites for reactant adsorption as well as distinct passivity to O<sub>2</sub> dissociation. Therefore, photoexcitation and surface catalysis present opposite dependence on Au NP size and codetermine the final photocatalytic performance in propylene oxidation. An integral consideration of the above two aspects should be instructive for a better understanding of SPR-enhanced photocatalysis and the design of efficient metal–semiconductor systems for ideal solar energy conversion.

**KEYWORDS:** surface plasmon resonance, surface catalysis, charge separation, energy transfer, photocatalytic oxidation, particle size, Au–CeO<sub>2</sub>



## INTRODUCTION

Recent years have seen a flourishing interest in semiconductor photocatalysis for harvesting and utilizing solar energy.<sup>1–6</sup> Photocatalysis is defined as the integration of photoexcitation and surface catalysis. Photoexcitation involves light absorption and charge output, while surface catalysis concerns the utilization of photoinduced carriers (e<sup>-</sup>/h<sup>+</sup>). In order to achieve solar to chemical energy conversion, above two sequential steps must be guaranteed concurrently. As such, the energy conversion efficiency ( $\eta$ ) is limited by the product of light-harvesting ( $\eta_{\text{LH}}$ ), charge output ( $\eta_{\text{CO}}$ ), and carrier utilization ( $\eta_{\text{CU}}$ ) efficiencies.<sup>3,7,8</sup> Recently, addition of small amounts of metals (e.g., Pt, Au, Ag) to semiconductors is found to be effective in facilitating photocatalytic H<sub>2</sub> production and organic oxidation.<sup>5,9–12</sup> The enhancements are largely explained by the surface plasmon resonance (SPR) of metallic nanostructures, which has been proposed to promote charge separation,<sup>13–15</sup> electron injection,<sup>9,16–19</sup> and resonant energy transfer.<sup>20–24</sup> SPR mainly concerns the photoexcitation step. On the other hand, for surface catalysis, Li's group has made

extensive efforts in exploring noble metals as reductive cocatalysts in photocatalytic water splitting.<sup>7,8,25,26</sup> Within those systems, loaded metals mostly catalyze electrons involved surface reactions, such as proton reduction, by lowering the activation energy of specific processes. For the present, the knowledge of metallic nanostructures in photocatalysis is multifarious and may be one-sided or even conflicting in some cases. It is necessary to explore an optimal equilibrium among various critical factors.

Specifically for SPR, the resonant wavelength and intensity depend on not only the nature but also the size and shape of metallic nanostructures.<sup>27–29</sup> Several mechanisms have been proposed to rationalize SPR-related positive roles in photocatalysis, as mentioned above. Although these mechanisms are not mutually exclusive, some of them are conditional and limited by selection rules. For charge separation, Ag and Au

Received: October 22, 2014

Revised: December 2, 2014

Published: December 10, 2014

exhibit capacitive properties for storing electrons from excited semiconductors, superior to Pt and Pd, which provide an ohmic contact.<sup>14,15,30</sup> Moreover, relatively small (<10 nm) metal nanoparticles (NPs) are more effective in storing electrons and negatively shifting the Fermi level.<sup>31–33</sup> For plasmonic electron injection, there is reported to be a threshold that only allows the transfer of high-energy electrons from Au NPs across the metal–semiconductor interfaces.<sup>34</sup> Again, the energy threshold is affected by the Fermi level equilibration between metals and semiconductors.<sup>34,35</sup> In addition, metallic SPR of large NPs (>50 nm) can be accompanied by an efficient scattering of resonant photons, which increases the probability of photon harvesting.<sup>29,36</sup> Understandably, various nature- and size-based selection rules usually result in nonconformity among different situations. According to the literature, larger Au NP loaded TiO<sub>2</sub> and CeO<sub>2</sub> show better activity under visible light toward the aerobic oxidation of benzyl alcohol (13–70 nm)<sup>37</sup> and 2-propanol (12–60 nm)<sup>38</sup> and hydrogen generation (30–70 nm).<sup>39</sup> However, in some other reports, excess and larger metal loading have a minor or even negative influence on photocatalysis.<sup>5,16,40,41</sup>

Essentially, metallic nanostructures show two distinctive features which separate them from semiconductors in photocatalysis. The first is that they effectively couple the light-harvesting and catalytic functions in one material. In contrast, semiconductors generally exhibit poor catalytic activity, owing to the lack of electron density near the Fermi level.<sup>12,42–44</sup> As such, loaded metals have been explored as cocatalysts for promoting the surface catalysis step. Since the late 1980s, Haruta et al. have revealed the excellent catalytic activity of loaded Au NPs with finite sizes (2–5 nm) toward CO oxidation under dark conditions.<sup>45–48</sup> Another unique feature is that plasmonic metals can integrate light flux and thermal energy to drive chemical reactions.<sup>49–51</sup> That is, higher temperatures bring about higher catalytic rates. In contrast, most semiconductor catalyzed reactions exhibit negative temperature dependence, owing to the decreased lifetime of photoexcited charge carriers caused by nonradiative and multiphonon recombination.<sup>52–55</sup>

In metal–semiconductor systems, in order to achieve an optimal equilibrium, various selection rules concerning photoexcitation and surface catalysis steps should be balanced. For example, the specific size of metal NPs may cause opposite influences on the above two steps, and there probably exists an optimal size range. As another example, plasmonic metals and most semiconductors exhibit inverse reaction rate dependence on temperature. Suppressed photocatalytic ethylene oxidation has been observed over TiO<sub>2</sub> at higher temperatures (>200 °C),<sup>52</sup> which can be met by plasmonic heating under xenon lamp or laser irradiation.<sup>50,56</sup> In order to bypass this conflict, herein we select CeO<sub>2</sub> as the metal NP supporter, within which the coupled electronic and ionic conduction help improve the negative temperature effect and couple light flux with thermal energy.<sup>53–55</sup> Through facile photodeposition, Au NPs with various sizes (3–20 nm) were loaded on CeO<sub>2</sub> nanorods. Aerobic oxidation of propylene under simulated sunlight and visible (>420 nm) light was selected as probe reactions. Modifications to the whole photocatalytic process brought about by Au loading have been integrally considered, including the SPR photoabsorption, charge separation, resonant energy transfer, and surface catalysis. It was found that photoexcitation and surface catalysis presented opposite dependence on Au NP size and codetermined the final photocatalytic performance.

Generally for an ideal solar energy conversion, medium Au particle sizes (6–12 nm), neither too small nor too large, should be used, equilibrating the plasmonic and catalytic roles over loaded metal NPs.

## ■ EXPERIMENTAL SECTION

**Chemicals and Characterization.** All reagents were of analytical purity and were used as received from Sinopharm Reagent Co. Ltd. The purity and crystallinity were characterized by powder X-ray diffraction (XRD) with a Rigaku D/MAX 2250 V diffractometer using monochromated Cu K $\alpha$  ( $\lambda$  = 0.15418 nm) radiation. The morphologies and microstructure characterizations were determined on a TecnaiG2 F20 S-Twin instrument. The actual Au content was measured by inductively coupled plasma atomic emission spectrometry (ICP-AES) with a VISTA instrument (Varian Co. USA). Diffuse reflectance spectra were obtained on a UV–vis spectrophotometer (Hitachi U-3010) using BaSO<sub>4</sub> as the reference. The N<sub>2</sub>-sorption measurements were performed at 77 K using a Micromeritics Tristar 3000 analyzer. X-ray photoelectron spectroscopy (XPS) analysis was performed on an ESCALAB 250 instrument (Thermo Scientific Ltd.). The C 1s signal was used to correct the charge effects. Room-temperature photoluminescence (PL) was recorded on a Hitachi F-4600 fluorescence spectrophotometer. Time-resolved fluorescence spectra were measured on a HORIBA Scientific Fluoro-Cube. The instrument worked on the principle of time-correlated single-photon counting (TCSPC). The oxygen temperature programmed desorption (O<sub>2</sub>-TPD) analysis of as-prepared Au-CeO<sub>2</sub> was performed on a Micromeritics ChemiSorb 2750 instrument, equipped with a thermal conductivity detector. For each sample (40 mg), after pretreatment with a He flow at 300 °C in a quartz reactor, the adsorption of O<sub>2</sub> was performed in a 4% O<sub>2</sub>/He gas flow for 1 h at room temperature. Afterward, the sample was heated to 850 °C at a heating rate of 10 °C min<sup>-1</sup> under a pure He gas flow.

**Materials Preparation.** CeO<sub>2</sub> nanorods were prepared by a mild hydrothermal method. Briefly, Ce(NO<sub>3</sub>)<sub>3</sub>·6H<sub>2</sub>O (3 mmol) was added to 40 mL of a NaOH (6 M) aqueous solution. The mixture was stirred for 30 min and transferred into a 50 mL Teflon-lined autoclave with a stainless steel tank. The autoclave was heated to 110 °C for 24 h. The precipitates obtained were rinsed several times with deionized water and anhydrous ethanol and then freeze-dried and oven-dried at 60 °C in air, successively. Finally, the powders were heated at 400 °C in air for 3 h before photocatalytic oxidation and characterization. Au NPs with various sizes (3–20 nm) were loaded on CeO<sub>2</sub> nanorods by photodeposition, altering the nominal content and concentration of chloroauric acid (HAuCl<sub>4</sub>) during the preparation process. Typically, 150 mg of CeO<sub>2</sub> powder was dispersed in a mixture of 30 mL of deionized water and 10 mL of methanol. Various contents of HAuCl<sub>4</sub> (0.25, 0.5, 0.67, and 1 wt %) were added to the above slurry and the mixtures were stirred for 3 h in the dark. Afterward, the solution was irradiated under a 15 W UV lamp for 8 min. As-prepared powders were rinsed to ensure the complete removal of Cl<sup>-</sup>. After filtration, the precipitates were freeze-dried and ready for subsequent operations.

**Photocatalytic Propylene Oxidation.** The catalytic activities of Au-CeO<sub>2</sub> samples (50 mg) were evaluated by aerobic oxidation of propylene (25 ppm), operated in a gas-closed vitreous reactor (capacity 650 mL) with a quartz window and a double-walled jacket. A Xe lamp (500 mW cm<sup>-2</sup>) and a

>420 nm filter were used to simulate the sunlight and visible light. During all propylene oxidation experiments, the reaction system temperature was kept at 50 °C using the circulating water, close to the equilibrium temperature of the photo-thermal effect over Au-CeO<sub>2</sub>. The oxidation process was monitored by the decrease of C<sub>3</sub>H<sub>6</sub> and the increase of CO<sub>2</sub> simultaneously, by GC analysis (GC 7900, Techcomp) equipped with two detective channels. The channel for C<sub>3</sub>H<sub>6</sub> and C<sub>3</sub>H<sub>8</sub> detection consists of a TM plot-Al<sub>2</sub>O<sub>3</sub>/S capillary column and a flame ionization detector (FID). Another channel for CO<sub>2</sub> detection consists of a TDX-01, 80–100 mesh packed column followed by a methane conversion furnace and a FID.

**Electrochemical Analysis.** The electrochemical analysis was performed on a CHI 660D electrochemical workstation (Shanghai Chenhua, People's Republic of China) using a standard three-electrode quartz cell. A Xe lamp (CHF-XM500) was used as a light source equipped with a high-pass filter (>510 nm). To make a working electrode, Au-CeO<sub>2</sub> powders were deposited on a 15 × 25 mm fluorine-doped tin oxide (FTO) substrate by Nafion coating. Briefly, 10 mg of catalyst was suspended in 400 μL of a 1 wt % Nafion–ethanol solution and the mixtures were ultrasonically scattered for 5 min. Then, 150 μL of the above slurry was coated on the FTO glass. After evaporation of ethanol, the catalyst-coated FTO substrate was used as the working electrode. The current–time curves were collected at open-circuit voltage. During the measurements, the electrolyte was 0.1 M Na<sub>2</sub>SO<sub>4</sub> solution (pH 6.8) that was bubbled with nitrogen.

## RESULTS AND DISCUSSION

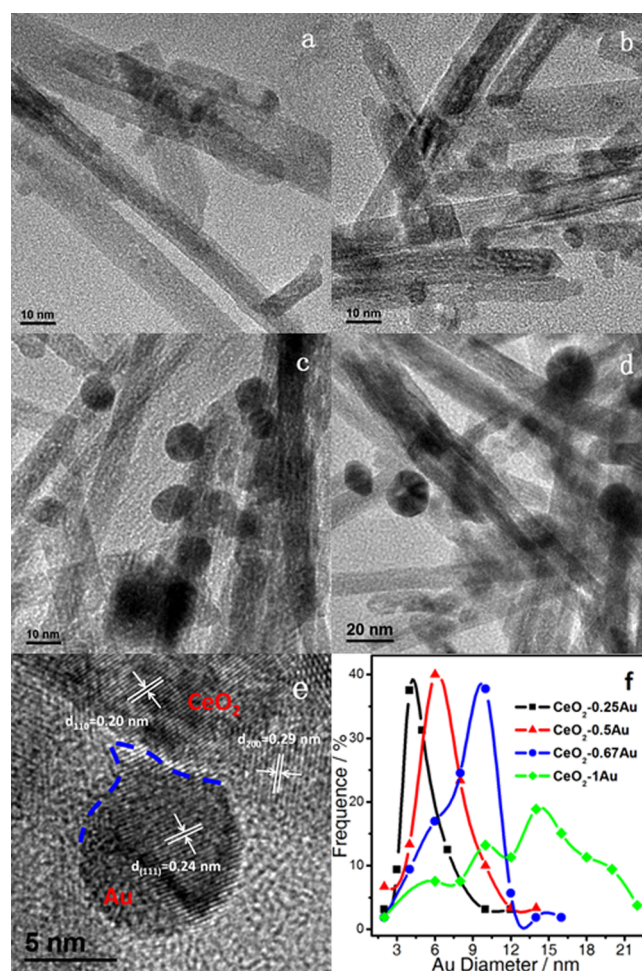
Various Au loading amounts (0.25–1 wt %) and particle sizes (3–20 nm) were regulated by altering the concentration of the precursor chloroauric acid (47.6–190 μM) during photo-deposition. The actual contents of attached Au NPs were determined by detecting the residual Au ions in the precursor solution with inductively coupled plasma (ICP) analysis and are summarized in Table 1. Notably, almost all of the added Au was

**Table 1. Actual Au Content from ICP Analysis and the Weighted Average Diameter and Surface Area of Supported Au NPs from Corresponding Size Distribution**

	sample			
	CeO <sub>2</sub> -0.25Au	CeO <sub>2</sub> -0.5Au	CeO <sub>2</sub> -0.67Au	CeO <sub>2</sub> -1Au
content (wt %)	0.24	0.48	0.64	0.93
diameter (nm)	4.9	6.8	8.4	13.6
surface area (m <sup>2</sup> g <sup>-1</sup> )	0.177	0.262	0.263	0.253

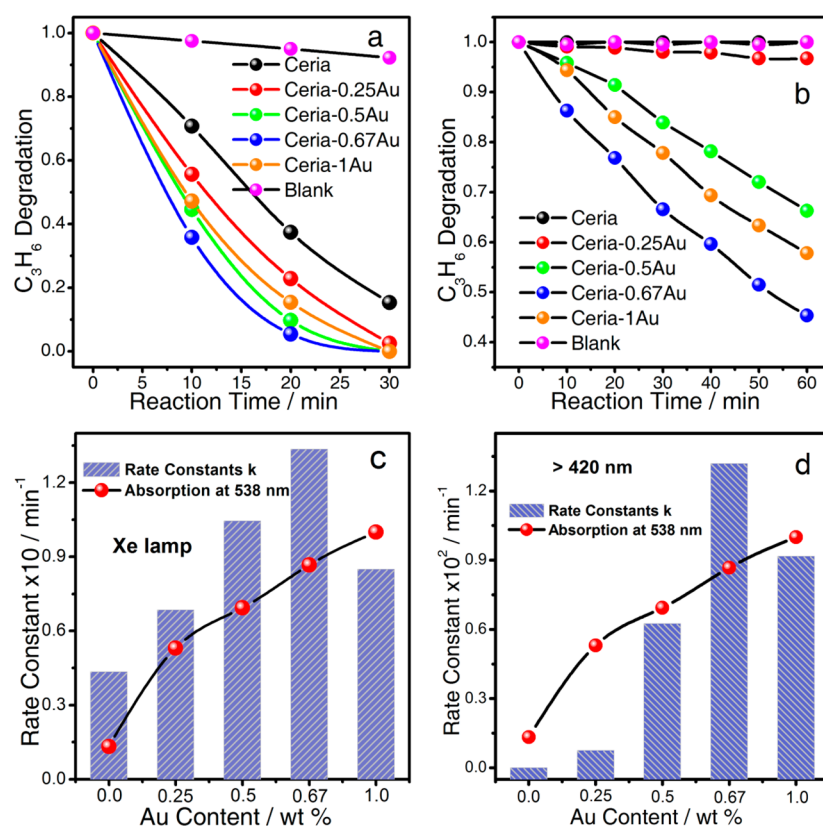
successfully loaded on the surface of CeO<sub>2</sub>. This can be attributed to the sufficient preadsorption before photo-deposition. Herein, for conciseness the samples were named according to the nominal content of Au. As characterized by X-ray diffraction (XRD), all Au-CeO<sub>2</sub> samples present exactly the same patterns as pristine CeO<sub>2</sub> (Figure S1, Supporting Information), readily indexed to a cubic fluorite structure (JCPDS 34-0394). Negligible structural modifications after Au attachment probably stem from the finite loading amount as well as the high dispersion of Au NPs on CeO<sub>2</sub>.

TEM (Figure 1 and Figure S2, Supporting Information) images indicate that Au NPs are well dispersed on the surface of ceria nanorods, which are 8–12 nm in diameter and 100–200 nm in length. The high-resolution version (Figure 1e) exhibits



**Figure 1.** (a–d) Transmission electron microscopy (TEM) images of 0.25 wt % (a), 0.5 wt % (b), 0.67 wt % (c), and 1 wt % (d) Au NP loaded CeO<sub>2</sub> nanorods. (e) High-resolution TEM image of a CeO<sub>2</sub>-0.67Au sample. Au-CeO<sub>2</sub> interfaces are marked by dotted lines. (f) Size distribution of Au NPs in the above Au-CeO<sub>2</sub> samples.

an interplanar spacing of 0.24 nm corresponding to the {111} planes of face-centered cubic (FCC) gold and a lattice spacing of 0.2 and 0.29 nm indexed to the exposed {110} and {200} facets of CeO<sub>2</sub>. By careful inspection of the metal–semiconductor interfaces (Figure 1e), an epitaxial heterojunction between the Au{111} and CeO<sub>2</sub>{110} planes is clearly discernible, indicating perfect contact between them. This close contact may help facilitate the charge as well as the energy transfer across the junction. The use of nonporous and crystalline CeO<sub>2</sub> supports enables a precise determination of the Au NP size distribution by inspection of a good number of TEM images. Notably (Figure 1f), with an increase of Au loading from 0.25 to 0.67 wt %, Au NPs roughly grow from 3–6 nm to 6–12 nm, with the nominal addition further reaches 1 wt %, Au NPs grow to 10–20 nm, with a relatively wide size distribution. As a result of Au loading, a broad SPR absorption peak appears around 400–800 nm with its center at ca. 538 nm (Figure S3, Supporting Information). An increase in metal NP size does not induce qualitative changes in the optical and electronic properties of Au-CeO<sub>2</sub> systems (Figure S3), though the plasmonic intensity increases with Au loading.<sup>34</sup> The increased photoabsorption from Au SPR may help enhance the harvesting of solar energy and promote related photocatalytic processes.



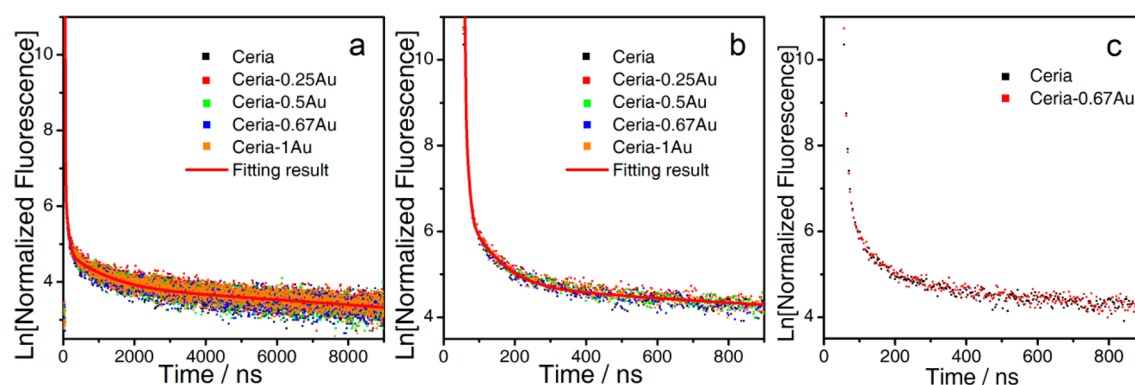
**Figure 2.** (a, b) Propylene (25 ppm) oxidation over Au-loaded CeO<sub>2</sub> under (a) simulated sunlight and (b) >420 nm light irradiation. (c, d) Apparent rate constants ( $k$ ) of propylene oxidation under (c) a Xe lamp and (d) visible light calculated by using pseudo-first-order reaction kinetics. Absorption at 538 nm was normalized using the SPR absorption of a CeO<sub>2</sub>-1Au sample (Figure S3, Supporting Information) as 1 unit.

Figure 2 presents the aerobic oxidation of propylene under simulated sunlight and visible light (>420 nm) irradiation. As monitored by gas chromatographic (GC) analysis, neither propane (C<sub>3</sub>H<sub>8</sub>) as a reductive hydrogenation product nor propylene oxide (PO) as an oxidative product could be traced during the photocatalytic process. The propylene oxidation cannot proceed in the dark (data not shown), clearly indicating the light-driven nature of this process. In addition, blank tests in the absence of any Au-CeO<sub>2</sub> samples were performed (Figure 2a,b). The photolysis of propylene contributed to less than 9% of propylene decrease under a Xe lamp and was not detectable under visible light, indicating the indispensable role of the catalyst powders in propylene oxidation. Furthermore, the same Au-CeO<sub>2</sub> sample after 20 h of Xe lamp irradiation was carefully studied by TEM (Figure S4, Supporting Information) and XPS (Figure S5, Supporting Information) analysis. The undetectable modifications on particle size and oxidation state of supported Au NPs as well as CeO<sub>2</sub> substrate indicate the stability of as-prepared catalysts, consistent with the undiminished performance after repeated photocatalytic cycles (Figure S6, Supporting Information).

Specifically, Figure 2a,c shows propylene oxidation over various Au-CeO<sub>2</sub> samples under simulated sunlight irradiation. The apparent rate constants ( $k$ ) were determined by linear estimation using pseudo-first-order reaction kinetics (Figure S7, Supporting Information). Notably, the propylene oxidation has been greatly promoted by loading finite Au NPs. The optimal performance was achieved over 0.67 wt % Au loaded CeO<sub>2</sub> nanorods, exhibiting more than 3-fold enhancement in comparison to the value for pristine CeO<sub>2</sub>. However, the propylene oxidation rate decreased significantly when Au

loading further reached 1 wt %. Notably, as shown in Figure 2c, this variation trend of photocatalytic performance with increased metal loading is inconsistent with that of the SPR photoabsorption. Under visible light (>420 nm) irradiation, the reaction rate dependence on Au loading amounts (Figure 2b,d) presented a humplike curve similar to that under simulated sunlight irradiation. The propylene oxidation rate increased with Au content and reached a maximum at 0.67 wt % loading, though the SPR-induced photoabsorption showed a linear growth until 1 wt % loading (Figure 2d). Some previous studies ascribe the depressed photocatalytic processes upon excess metal loading to strong photon scattering,<sup>34</sup> charge recombination,<sup>16</sup> etc.<sup>5,15</sup> However, those reports have rarely taken surface catalysis involving the metal into serious consideration, which plays a decisive role in photocatalysis. Hereafter, in order to probe the origin of the above humplike trends, various factors involved in both photoexcitation and surface catalysis steps after Au addition are integrally discussed, including the photoinduced carrier lifetime, charge separation, resonant energy transfer, and surface catalysis.

Photoluminescence (PL) spectra have been widely used to explore the fate of excited charge (e<sup>-</sup>/h<sup>+</sup>) pairs in semiconductors because PL emission results from the recombination of free carriers. Figure S8 in the Supporting Information shows the room-temperature PL of various Au loaded CeO<sub>2</sub> samples, with 340 nm light excitation, in the range of 400–540 nm. All samples exhibit broad emission containing several subpeaks, which are attributed to various kinds of defects related to charge recombination.<sup>57</sup> Obviously, Au loading induces distinct decreases in PL intensity, widely explained by a lower recombination rate of electron–hole (e<sup>-</sup>/h<sup>+</sup>) pairs under



**Figure 3.** Time-resolved fluorescence decay detected at 470 nm with an excitation wavelength of 340 nm over different Au loaded CeO<sub>2</sub> samples, presented with different time scales (a, b) and different comparison samples (c).

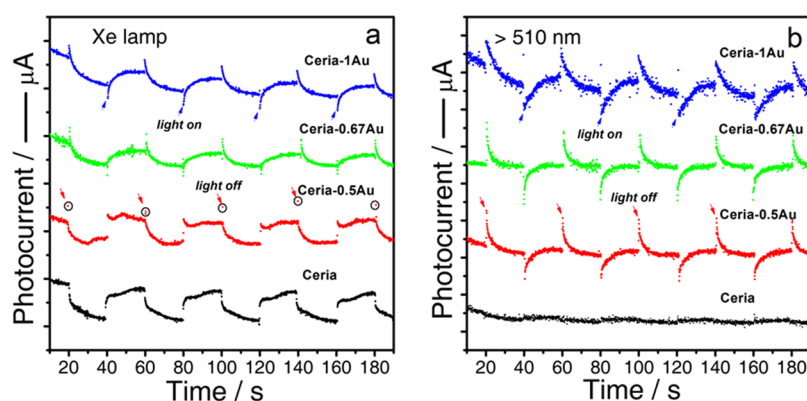


**Figure 4.** Transient current–time ( $i-t$ ) curves of various Au loaded CeO<sub>2</sub> electrodes recorded under (a) Xe lamp and (b) visible (>510 nm) light irradiation.

light irradiation.<sup>3,58</sup> The PL intensity gradually decreases with an increase of Au addition, and CeO<sub>2</sub>-1Au presents the most depressed signal. Given the previously proposed charge trapping role of Au NPs, the variation trend of PL emission agrees with that of Au SPR absorption (Figure S3, Supporting Information), which cannot adequately explain the hump-like activity curve in Figure 2.

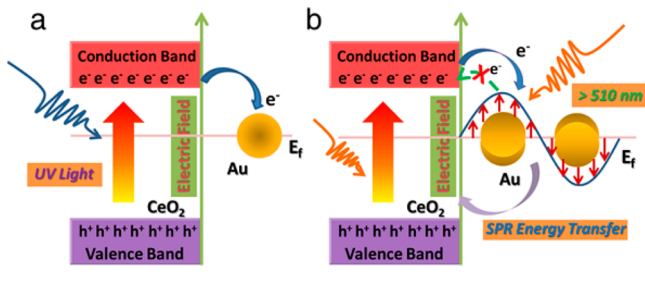
However, some studies have reported the light shielding and photon scattering effect of supported metal NPs, inducing inaccuracy and misjudgment in PL analysis.<sup>21</sup> To further understand the fate of excited charges in CeO<sub>2</sub> in the presence of Au NP loading, time-resolved fluorescence decay studies were performed (Figure 3 and Figure S9, Supporting Information), disclosing useful information about exciton lifetime.<sup>59,60</sup> Notably with all Au loaded CeO<sub>2</sub> samples, fluorescence decay from CeO<sub>2</sub> has not been obviously modified by the presence of metal NPs on its surface (Figure 3a). Furthermore, a similar phenomenon was observed using different time resolution (Figure 3b), different detection wavelength (Figure S9), and a careful comparison of the transient decay of pure CeO<sub>2</sub> and CeO<sub>2</sub>-0.67Au (Figure 3c), which exhibited the optimum performance in propylene oxidation (Figure 2). The above results indicate that Au NP loading does not effectively prolong the lifetime of excited carriers, though the charge recombination process seems to be quenched according to the PL data (Figure S8, Supporting Information). The lack of changes in semiconductor carrier dynamics with supported metals has been reported to be general. A similar phenomenon was observed with Au or Pt loaded P25 (TiO<sub>2</sub>) in different environments and with various

metal loadings.<sup>59</sup> Given the fluorescence decay studies, Au NP attachment to CeO<sub>2</sub> makes a minor contribution to promoting the electron transfer, even if it does aid in photocatalysis. That is, metal SPR mediated charge separation probably plays only a part of the crucial role in determining the final performance of photocatalytic propylene oxidation.

In addition to the above photophysics analysis, the transient photocurrent (Figure 4) provides us with more visual evidence on electron (e<sup>-</sup>) transfer and injection within metal–semiconductor systems. Figure 4a indicates that CeO<sub>2</sub> and various Au loaded CeO<sub>2</sub> electrodes present obvious but varied current switches via on–off cycles of Xe lamp irradiation. Pristine CeO<sub>2</sub> presents a gradually rising current when the light is on and a declining signal when the light is off. This kind of transient delay stems from the electron trapping and releasing mediated by surface defects. Notably, in the presence of Au NP attachment, the corresponding current switches change a great deal. For example, as circled in Figure 4a, the transient current of CeO<sub>2</sub>-0.5Au exhibits obvious charge release once the light is shielded, indicating sufficient charge storage on exposure to photons (Scheme 1a). In comparison with the signal of pristine CeO<sub>2</sub>, the above charge storage and release should be reasonably attributed to Au NPs addition.<sup>13–15</sup> With an increase of Au loading to 0.67 and 1 wt %, the charge storage and release processes are further enhanced such that the current signals present an instantaneous decline when the light is switched on and an exceptional rise when the light is switched off (Figure 4a).

Figure 4b presents the transient current–time curves under visible (>510 nm) light irradiation, which is in accordance with

**Scheme 1. Schematic Representation of the Charge Transfer within Au Loaded CeO<sub>2</sub> Systems on Irradiation by (a) UV and (b) >510 nm Visible Light**



the plasmonic absorption of supported Au NPs (Figure S3). As expected, pristine CeO<sub>2</sub> gives negligible transient current responses because of its weak absorption in >510 nm region. After finite loading of Au NPs, the periodic on/off current responses are greatly enhanced over all Au-CeO<sub>2</sub> samples (Figure 4b). Notably, all three Au-CeO<sub>2</sub> (0.5–1 wt %) coated electrodes present similar charge storage and release under Xe lamp irradiation (Figure 4a), indicating the lack of participation of electron injection from SPR Au NPs into CeO<sub>2</sub>. This phenomenon is probably due to two reasons, as depicted in Scheme 1b: (1) the near-field resonant energy transfer from SPR Au NPs greatly increases the steady-state population of energetic charge carriers in adjacent CeO<sub>2</sub>;<sup>20–24</sup> (2) there exists a threshold energy ( $E_T$ ) which only allows the transfer of high-energy plasmonic electrons across Au-CeO<sub>2</sub> interfaces, hardly supplied by >510 nm photons.<sup>34</sup> In summary, with an increase of Au loading (0.25–1 wt %) as well as NP size (3–20 nm), there is no recession in the charge separation and resonant energy transfer. In combination with the above photophysics data and humplike activity dependence, it can be concluded that the photoexcitation step (i.e., light absorption and charge output) only partially determine the final photocatalytic efficiency.

After careful examination of photoexcitation-related processes, we cannot roughly ascribe the degraded performance upon excess Au loading (1 wt %) to photon scattering and charge recombination. In order to achieve an optimal solar to chemical energy conversion, surface catalysis must be taken into consideration simultaneously. Loaded metals serving as proton reduction cocatalysts have proven to be effective in promoting the utilization of excited carriers ( $e^-$ ).<sup>8</sup> Recently, Joo et al. proposed the promotion of atomic hydrogen recombination as an alternative to electron trapping for the role of metals (Au) in photocatalytic H<sub>2</sub> production.<sup>59</sup> The above reports mostly focused on metals in half-reactions involving electrons. Especially, the cocatalyst related viewpoint is based on effective electron trapping at metal sites. At present, the discussion concerning the catalytic role of metal loading in photocatalytic oxidation has been deficient. This current situation is mainly due to the inherent superiority of metals in electron extraction and storage when they are in contact with excited semiconductors. However, in some photooxidation reactions, such as propylene oxidation in this study, the humplike activity dependence indicates that metal loading probably influences the surface catalysis step as well.<sup>37,61,62</sup> Before probing the catalytic roles of Au NPs in photocatalytic propylene oxidation over Au-CeO<sub>2</sub>, we examined the valence state of supported Au NPs, which has proved to influence the charge transfer as well as surface catalysis.<sup>58,63,64</sup> As shown in Figure S10 in the

Supporting Information, the X-ray photoelectron spectra (XPS) of various Au (0.5–1 wt %) loaded CeO<sub>2</sub> samples present identical Au<sub>4f7/2</sub> and Au<sub>4f5/2</sub> signals located at 83.4 and 87.0 eV, indicating the metallic nature of Au<sup>0</sup> within all the samples. Therefore, the valence derived activity difference in the above propylene oxidation over Au modified CeO<sub>2</sub> can be excluded to some extent.

In order to explore the credible roles of supported Au in surface catalysis, particle size and surface area should be considered. As shown in Table 1 and Figure 5, the weighted

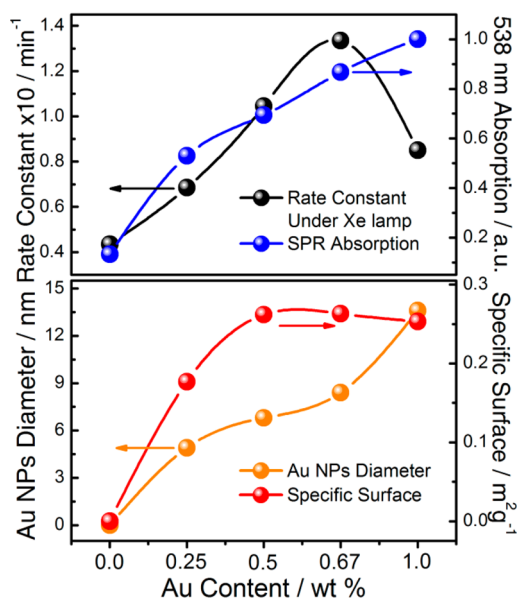


**Figure 5.** Integrated correlations among Au NP loading amounts, particle size, plasmonic absorption, specific surface area of Au, and rate constant of propylene oxidation over various Au loaded CeO<sub>2</sub> samples.

average diameter and surface area of supported Au NPs were calculated (eqs S1–S8, Supporting Information), on the basis of the actual metal contents (Table 1) and corresponding size distribution (Figure 1f). It is clearly indicated that, with the increase of Au content, the specific surface area of Au presents an increase at first and tends to be saturated at 0.67 wt % loading, due to the continuous increase of Au NP size. Higher metal loadings (1 wt %) even induce a slight decrease of exposed Au area from 0.26 to 0.25 m<sup>2</sup> g<sup>-1</sup> catalyst (Figure 5). Given the humplike activity curve in the photocatalytic oxidation of propylene (Figure 2), it is reasonable to infer that the stagnation of Au surface area leads to a decrease in exposed active sites, thus resulting in the depressed photooxidation. However, the slightly decreased surface area cannot be solely responsible for such a collapsed performance upon 1 wt % Au loading. There should be another determinant in the surface catalysis involving Au, probably related to the size of loaded metals. Oversized Au NPs on various oxide supporters have been widely accepted to be useless in thermocatalysis.<sup>45–48</sup> Notably (Figure 5), the weighted average diameter of Au NPs reaches ca. 13.6 nm at 1 wt % loading, while the other Au (0.25–0.67 wt %) loaded CeO<sub>2</sub> has finer metal sizes below 10 nm. With an increase of Au diameter, especially when it exceeds 10 nm, the external surfaces of Au NPs become smoother and less defective. Such clean Au clusters evidently present chemical passivity to the adsorption and activation of oxygen as well as olefins, such as ethylene and acety-

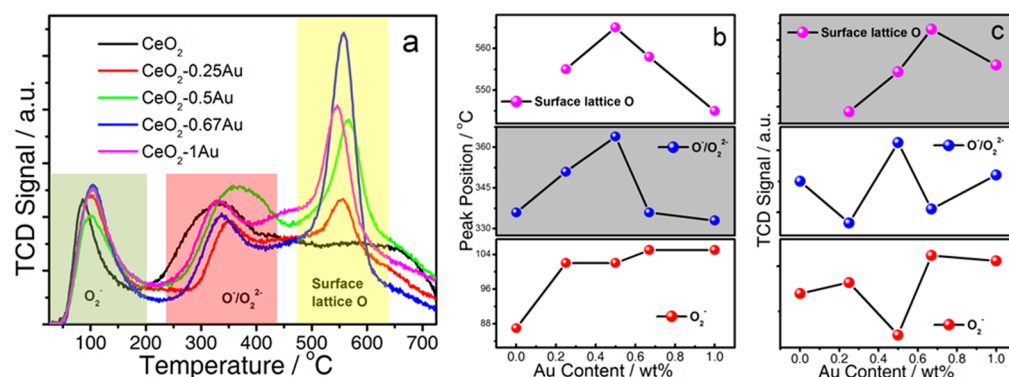


**Figure 6.** (a) O<sub>2</sub>-TPD profiles of the Au-CeO<sub>2</sub> catalysts with different Au loading amounts. (b, c) Summaries of the three separated oxygen desorption peaks according to their (b) temperature positions and (c) TCD signals.

lene.<sup>10,45,59,63,65</sup> The degraded reactant activation probably gives rise to a frustrating catalytic activity in the propylene photooxidation, due to the modifications of charge transfer from excited metals to adsorbed molecules.<sup>66,67</sup>

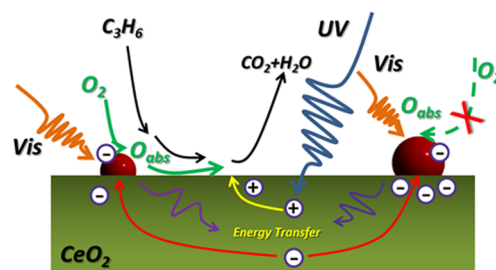
In order to further understand the suppressed surface catalysis on account of outgrown metal NPs, oxygen temperature-programmed desorption (O<sub>2</sub>-TPD) analysis was performed. It provides us with an opportunity to get insight into the adsorbed oxygen species, as well as the mobility of corresponding surface-active sites.<sup>68,69</sup> As shown in Figure 6a, the pure CeO<sub>2</sub> mainly presents two O<sub>2</sub> desorption peaks at 90 and 336 °C, which can be ascribed to the adsorbed superoxide (O<sub>2</sub><sup>-</sup>) and peroxide (O<sup>-</sup>) species, respectively.<sup>69,70</sup> The chemical adsorption of molecular O<sub>2</sub> on the CeO<sub>2</sub> surface stems from the abundant surface vacancies, analogous to the case of TiO<sub>2</sub>.<sup>71,72</sup> Notably, with finite Au (0.25–1 wt %) NP loading, the O<sub>2</sub>-TPD curves change a great deal. In addition to the weakly bonded superoxide (O<sub>2</sub><sup>-</sup>) species around 100 °C and the peroxide (O<sup>-</sup>) species probably transferred from supported Au NPs to adjacent vacancies (300–400 °C), Au additions give rise to another distinct peak around 550 °C, attributed to the desorption of surface lattice oxygen.<sup>72,73</sup> That is, loading Au NPs greatly enhances the surface mobility of lattice oxygen within the CeO<sub>2</sub> supporter.

Furthermore, the O<sub>2</sub>-TPD profiles of all Au-CeO<sub>2</sub> samples are unscrambled in detail according to the temperature positions (Figure 6b) and TCD signals (Figure 6c) of the three desorption peaks. Herein for a valid conclusion, two evident points are extracted, though some other valuable information may be concealed in the interlaced curves. (1) With an increase of Au loading (Figure 6b), the second desorption peak assigned to surface peroxide (O<sup>-</sup>) species shifts to higher temperature at first and shifts to lower temperature when the Au content exceeds 0.5 wt %. That is, CeO<sub>2</sub>-0.5Au gives the most stable peroxide (O<sup>-</sup>) species while higher Au loadings induce weaker bonding, comparable to that of pristine CeO<sub>2</sub>. Previous reports have proved that CeO<sub>2</sub> nanorods presenting superior activity toward the total oxidation of CO and hydrocarbons have more stable O<sub>2</sub> chemisorption in comparison to CeO<sub>2</sub> nanocubes.<sup>69,70,74,75</sup> It is reasonable to ascribe the suppressed oxygen activation to the increased chemical passivity of outgrown metals NPs. (2) The mobility of surface lattice oxygen has been greatly promoted after loading Au NPs (Figure 6a). The enhancement can be determined by the area of the desorption peak around 550 °C. Herein, the peak values of the TCD signal were roughly taken as criteria. Obviously in Figure 6c the oxygen mobility gradually increases

with Au addition and reaches a maximum at 0.67 wt % loading. A distinct degradation happens when the Au content further reaches 1 wt %, presenting a humplike trend similar to that of propylene oxidation. Given that Au loading did not change the crystalline structure or the electronic properties of CeO<sub>2</sub>, the variations in lattice oxygen mobility probably stem from the continuously increasing size of Au NPs and have an effect on the surface catalysis.

On the basis of the above integrated consideration of a series of critical factors in photocatalysis, we postulate a tentative reaction mechanism for the light-driven propylene oxidation (Scheme 2). When Au-CeO<sub>2</sub> is exposed to solar irradiation, UV

#### Scheme 2. Proposed Mechanism of the Aerobic Oxidation of Propylene over Au Loaded CeO<sub>2</sub> Nanorods under Solar Irradiation



photon packing energy that is no less than the band gap of CeO<sub>2</sub> will excite the semiconductor, with the generation of energetic e<sup>-</sup>/h<sup>+</sup> pairs. Meanwhile, the supported Au NPs play multiple roles in prompting the whole photocatalytic process: (1) Au NPs serve as electron trappers and improve the charge separation to some extent; (2) localized SPR within Au NPs makes them photon antennas for visible light harvesting and induces resonant energy transfer to adjacent CeO<sub>2</sub>; (3) external surfaces of Au NPs provide a platform for the adsorption of polar propylene molecules and subsequent reaction with oxygen; (4) excited plasmons on Au NPs act to populate O<sub>2</sub> antibonding orbitals and facilitate the rate-limiting O<sub>2</sub> dissociation, which has been proved both experimentally and computationally.<sup>10,51,61,63</sup> With an increase in Au loading and particle size, the first two roles involved in the photoexcitation step may be enhanced. However, the last two roles concerning the surface catalysis step will probably be greatly depressed when the Au NPs outgrow a suitable size (<10 nm). In summary, medium Au particle sizes (6–12 nm), neither too small nor too large, should be used, equilibrating the plasmon

and catalytic roles over metallic nanostructures. An integral consideration of the above two aspects makes the humplike activity curve in propylene oxidation reasonable and should be instructive in designing efficient SPR enhanced photocatalysts with an optimal equilibrium for ideal solar energy conversion.

## CONCLUSION

A series of Au modified CeO<sub>2</sub> samples were prepared by photodeposition, with various loading amounts (0.25–1 wt %) and particle sizes (3–20 nm). Aerobic oxidation of propylene under simulated sunlight and visible light was performed, to explore the decisive roles Au NPs play in photocatalytic oxidation. Modifications brought by Au attachment have been integrally discussed, concerning both the photoexcitation and surface catalysis steps. SPR mediated electron injection was absent between Au and CeO<sub>2</sub>, probably limited by the transfer threshold energy ( $E_T$ ). With the increase of Au loadings, the photoabsorption, charge separation, and resonant energy transfer seem to be promoted due to the enhanced Au SPR. However, increased Au sizes will lead to the saturation and even decrease of exposed active sites for the adsorption of reaction species. Furthermore, outgrown Au NPs (>10 nm) present distinct passivity to O<sub>2</sub> dissociation and activation. The opposite dependences of photoexcitation and surface catalysis on Au content result in an optimal equilibrium at 0.67 wt % loading, corresponding to the peak of the humplike curve in propylene oxidation. Generally, to design efficient metal–semiconductor systems for ideal solar energy conversion, medium particle sizes (6–12 nm) are required for equilibrating the plasmonic and catalytic roles over metallic nanostructures.

## ASSOCIATED CONTENT

### Supporting Information

The following file is available free of charge on the ACS Publications website at DOI: 10.1021/cs501633q.

XRD patterns of Au-CeO<sub>2</sub>, TEM image of CeO<sub>2</sub>-0.5Au and CeO<sub>2</sub> nanorods, DRS and PL spectra of Au-CeO<sub>2</sub>, linear estimation of apparent rate constants, stability tests of CeO<sub>2</sub>-0.67Au sample, time-resolved fluorescence decay and XPS of Au-CeO<sub>2</sub>, and calculation details of Au surface area (PDF)

## AUTHOR INFORMATION

### Corresponding Author

\*E-mail for W.W.: wzwang@mail.sic.ac.cn.

### Notes

The authors declare no competing financial interest.

## ACKNOWLEDGMENTS

We acknowledge financial support from the National Basic Research Program of China (2013CB933203) and the National Natural Science Foundation of China (51272269, 51272303, and 51102262).

## REFERENCES

- (1) Chen, X.; Shen, S.; Guo, L.; Mao, S. S. *Chem. Rev.* **2010**, *110*, 6503–6570.
- (2) Hou, W.; Cronin, S. B. *Adv. Funct. Mater.* **2013**, *23*, 1612–1619.
- (3) Ma, Y.; Wang, X.; Jia, Y.; Chen, X.; Han, H.; Li, C. *Chem. Rev.* **2014**, *114*, 9987–10043.
- (4) Maeda, K. *ACS Catal.* **2013**, *3*, 1486–1503.

- (5) Murdoch, M.; Waterhouse, G.; Nadeem, M.; Metson, J.; Keane, M.; Howe, R.; Llorca, J.; Idriss, H. *Nat. Chem.* **2011**, *3*, 489–492.
- (6) Lang, X.; Chen, X.; Zhao, J. *Chem. Soc. Rev.* **2014**, *43*, 473–486.
- (7) Li, R.; Han, H.; Zhang, F.; Wang, D.; Li, C. *Energy Environ. Sci.* **2014**, *7*, 1369–1376.
- (8) Yang, J.; Wang, D.; Han, H.; Li, C. *Acc. Chem. Res.* **2013**, *46*, 1900–1909.
- (9) Nishijima, Y.; Ueno, K.; Kotake, Y.; Murakoshi, K.; Inoue, H.; Misawa, H. *J. Phys. Chem. Lett.* **2012**, *3*, 1248–1252.
- (10) Christopher, P.; Xin, H.; Linic, S. *Nat. Chem.* **2011**, *3*, 467–472.
- (11) Atwater, H. A.; Polman, A. *Nat. Mater.* **2010**, *9*, 205–213.
- (12) Linic, S.; Christopher, P.; Ingram, D. B. *Nat. Mater.* **2011**, *10*, 911–921.
- (13) Costi, R.; Cohen, G.; Salant, A.; Rabani, E.; Banin, U. *Nano Lett.* **2009**, *9*, 2031–2039.
- (14) Costi, R.; Saunders, A. E.; Elmalem, E.; Salant, A.; Banin, U. *Nano Lett.* **2008**, *8*, 637–641.
- (15) Takai, A.; Kamat, P. V. *ACS Nano* **2011**, *5*, 7369–7376.
- (16) Primo, A.; Marino, T.; Corma, A.; Molinari, R.; Garcia, H. *J. Am. Chem. Soc.* **2011**, *133*, 6930–6933.
- (17) Nishijima, Y.; Ueno, K.; Yokota, Y.; Murakoshi, K.; Misawa, H. *J. Phys. Chem. Lett.* **2010**, *1*, 2031–2036.
- (18) Tian, Y.; Tatsuma, T. *J. Am. Chem. Soc.* **2005**, *127*, 7632–7637.
- (19) Jain, P. K.; Lee, K. S.; El-Sayed, I. H.; El-Sayed, M. A. *J. Phys. Chem. B* **2006**, *110*, 7238–7248.
- (20) Kulkarni, A. P.; Noone, K. M.; Munechika, K.; Guyer, S. R.; Ginger, D. S. *Nano Lett.* **2010**, *10*, 1501–1505.
- (21) Liu, Z.; Hou, W.; Pavaskar, P.; Aykol, M.; Cronin, S. B. *Nano Lett.* **2011**, *11*, 1111–1116.
- (22) Kumar, M. K.; Krishnamoorthy, S.; Tan, L. K.; Chiam, S. Y.; Tripathy, S.; Gao, H. *ACS Catal.* **2011**, *1*, 300–308.
- (23) Ingram, D. B.; Linic, S. *J. Am. Chem. Soc.* **2011**, *133*, 5202–5205.
- (24) Awazu, K.; Fujimaki, M.; Rockstuhl, C.; Tominaga, J.; Murakami, H.; Ohki, Y.; Yoshida, N.; Watanabe, T. *J. Am. Chem. Soc.* **2008**, *130*, 1676–1680.
- (25) Yan, H.; Yang, J.; Ma, G.; Wu, G.; Zong, X.; Lei, Z.; Shi, J.; Li, C. *J. Catal.* **2009**, *266*, 165–168.
- (26) Yang, J.; Yan, H.; Wang, X.; Wen, F.; Wang, Z.; Fan, D.; Shi, J.; Li, C. *J. Catal.* **2012**, *290*, 151–157.
- (27) Link, S.; El-Sayed, M. A. *J. Phys. Chem. B* **1999**, *103*, 4212–4217.
- (28) El-Sayed, M. A. *Acc. Chem. Res.* **2001**, *34*, 257–264.
- (29) Burda, C.; Chen, X.; Narayanan, R.; El-Sayed, M. A. *Chem. Rev.* **2005**, *105*, 1025–1102.
- (30) Harris, C.; Kamat, P. V. *ACS Nano* **2010**, *4*, 7321–7330.
- (31) Chen, S.; Ingram, R. S.; Hostetler, M. J.; Pietron, J. J.; Murray, R. W.; Schaaff, T. G.; Khoury, J. T.; Alvarez, M. M.; Whetten, R. L. *Science* **1998**, *280*, 2098–2101.
- (32) Jakob, M.; Levanon, H.; Kamat, P. V. *Nano Lett.* **2003**, *3*, 353–358.
- (33) Subramanian, V.; Wolf, E. E.; Kamat, P. V. *J. Am. Chem. Soc.* **2004**, *126*, 4943–4950.
- (34) Long, J.; Chang, H.; Gu, Q.; Xu, J.; Fan, L.; Wang, S.; Zhou, Y.; Wei, W.; Huang, L.; Wang, X.; Liu, P.; Huang, W. *Energy Environ. Sci.* **2014**, *7*, 973–977.
- (35) Liu, Z.-P.; Gong, X.-Q.; Kohanoff, J.; Sanchez, C.; Hu, P. *Phys. Rev. Lett.* **2003**, *91*, 266102.
- (36) Evanoff, D. D.; Chumanov, G. *ChemPhysChem* **2005**, *6*, 1221–1231.
- (37) Tanaka, A.; Hashimoto, K.; Kominami, H. *Chem. Commun.* **2011**, *47*, 10446–10448.
- (38) Kowalska, E.; Mahaney, O. O. P.; Abe, R.; Ohtani, B. *Phys. Chem. Chem. Phys.* **2010**, *12*, 2344–2355.
- (39) Seh, Z. W.; Liu, S.; Low, M.; Zhang, S.-Y.; Liu, Z.; Mlayah, A.; Han, M.-Y. *Adv. Mater.* **2012**, *24*, 2310–2314.
- (40) Li, H. X.; Bian, Z. F.; Zhu, J.; Huo, Y. N.; Li, H.; Lu, Y. F. *J. Am. Chem. Soc.* **2007**, *129*, 4538–4539.
- (41) Tsukamoto, D.; Shiraiishi, Y.; Sugano, Y.; Ichikawa, S.; Tanaka, S.; Hirai, T. *J. Am. Chem. Soc.* **2012**, *134*, 6309–6315.

- (42) Hammer, B.; Norskov, J. *Nature* **1995**, *376*, 238–240.
- (43) Nikolla, E.; Schwank, J.; Linic, S. *J. Am. Chem. Soc.* **2009**, *131*, 2747–2754.
- (44) Linic, S.; Christopher, P.; Xin, H.; Marimuthu, A. *Acc. Chem. Res.* **2013**, *46*, 1890–1899.
- (45) Haruta, M. *Catal. Today* **1997**, *36*, 153–166.
- (46) Haruta, M. *Nature* **2005**, *437*, 1098–1099.
- (47) Haruta, M.; Tsubota, S.; Kobayashi, T.; Kageyama, H.; Genet, M. J.; Delmon, B. *J. Catal.* **1993**, *144*, 175–192.
- (48) Hayashi, T.; Tanaka, K.; Haruta, M. *J. Catal.* **1998**, *178*, 566–575.
- (49) Adleman, J. R.; Boyd, D. A.; Goodwin, D. G.; Psaltis, D. *Nano Lett.* **2009**, *9*, 4417–4423.
- (50) Hung, W. H.; Aykol, M.; Valley, D.; Hou, W.; Cronin, S. B. *Nano Lett.* **2010**, *10*, 1314–1318.
- (51) Christopher, P.; Xin, H. L.; Marimuthu, A.; Linic, S. *Nat. Mater.* **2012**, *11*, 1044–1050.
- (52) Westrich, T. A.; Dahlberg, K. A.; Kaviani, M.; Schwank, J. W. *J. Phys. Chem. C* **2011**, *115*, 16537–16543.
- (53) Jiang, D.; Wang, W.; Gao, E.; Zhang, L.; Sun, S. *J. Phys. Chem. C* **2013**, *117*, 24242–24249.
- (54) Li, Y.; Sun, Q.; Kong, M.; Shi, W.; Huang, J.; Tang, J.; Zhao, X. *J. Phys. Chem. C* **2011**, *115*, 14050–14057.
- (55) Jiang, D.; Wang, W.; Zhang, L.; Qiu, R.; Sun, S.; Zheng, Y. *Appl. Catal., B* **2015**, *165*, 399–407.
- (56) Meng, X.; Wang, T.; Liu, L.; Ouyang, S.; Li, P.; Hu, H.; Kako, T.; Iwai, H.; Tanaka, A.; Ye, J. *Angew. Chem., Int. Ed.* **2014**, *126*, 11662–11666.
- (57) Jiang, D.; Wang, W.; Gao, E.; Sun, S.; Zhang, L. *Chem. Commun.* **2014**, *50*, 2005–2007.
- (58) Li, X. Z.; Li, F. B. *Environ. Sci. Technol.* **2001**, *35*, 2381–2387.
- (59) Joo, J. B.; Dillon, R.; Lee, I.; Yin, Y.; Bardeen, C. J.; Zaera, F. *Proc. Natl. Acad. Sci. U.S.A.* **2014**, *111*, 7942–7947.
- (60) Sun, S.; Wang, W.; Jiang, D.; Zhang, L.; Li, X.; Zheng, Y.; An, Q. *Nano Res.* **2014**, *7*, 1497–1506.
- (61) Chen, X.; Zhu, H. Y.; Zhao, J. C.; Zheng, Z. F.; Gao, X. P. *Angew. Chem.* **2008**, *120*, 5433–5436.
- (62) Tanaka, A.; Hashimoto, K.; Kominami, H. *J. Am. Chem. Soc.* **2012**, *134*, 14526–14533.
- (63) Wang, Y.-G.; Yoon, Y.; Glezakou, V.-A.; Li, J.; Rousseau, R. J. *Am. Chem. Soc.* **2013**, *135*, 10673–10683.
- (64) Subramanian, V.; Wolf, E. E.; Kamat, P. V. *Langmuir* **2003**, *19*, 469–474.
- (65) Su, R.; Tiruvalam, R.; He, Q.; Dimitratos, N.; Kesavan, L.; Hammond, C.; Lopez-Sanchez, J. A.; Bechstein, R.; Kiely, C. J.; Hutchings, G. J.; Besenbacher, F. *ACS Nano* **2012**, *6*, 6284–6292.
- (66) Lindstrom, C. D.; Zhu, X. Y. *Chem. Rev.* **2006**, *106*, 4281–4300.
- (67) Xiao, Q.; Sarina, S.; Bo, A.; Jia, J.; Liu, H.; Arnold, D. P.; Huang, Y.; Wu, H.; Zhu, H. *ACS Catal.* **2014**, *4*, 1725–1734.
- (68) Ma, C. Y.; Mu, Z.; Li, J. J.; Jin, Y. G.; Cheng, J.; Lu, G. Q.; Hao, Z. P.; Qiao, S. Z. *J. Am. Chem. Soc.* **2010**, *132*, 2608–2613.
- (69) Wu, Z.; Li, M.; Howe, J.; Meyer, H. M.; Overbury, S. H. *Langmuir* **2010**, *26*, 16595–16606.
- (70) Guo, J.; Shi, Z.; Wu, D.; Yin, H.; Gong, M.; Chen, Y. *Appl. Surf. Sci.* **2013**, *273*, 527–535.
- (71) Setvín, M.; Aschauer, U.; Scheiber, P.; Li, Y.-F.; Hou, W.; Schmid, M.; Selloni, A.; Diebold, U. *Science* **2013**, *341*, 988–991.
- (72) Ouyang, L.; Da, G.-j.; Tian, P.-f.; Chen, T.-y.; Liang, G.-d.; Xu, J.; Han, Y.-F. *J. Catal.* **2014**, *311*, 129–136.
- (73) Ma, L.; Wang, D.; Li, J.; Bai, B.; Fu, L.; Li, Y. *Appl. Catal., B* **2014**, *148–149*, 36–43.
- (74) Mann, A. K. P.; Wu, Z.; Calaza, F. C.; Overbury, S. H. *ACS Catal.* **2014**, *4*, 2437–2448.
- (75) Wu, Z.; Li, M.; Overbury, S. H. *J. Catal.* **2012**, *285*, 61–73.